# Volcanic lightning reveals umbrella cloud dynamics of the January 2022 Hunga Tonga-Hunga Ha'apai eruption

P. A. Jarvis[1*], T. G. Caldwell[1], C. Noble[2], Y. Ogawa[3], C. Vagasky[4]

1. GNS Science, PO Box 30368, Lower Hutt 5040, New Zealand
2. MetService, PO Box 722, Wellington 6140, New Zealand
3. Volcanic Fluid Research Centre, Tokyo Institute of Technology, Tokyo, Japan
4. Vaisala Inc., Louisville, Colorado

*Corresponding author: p.jarvis@gns.cri.nz

## Abstract

The 15 January 2022 eruption of Hunga Tonga-Hunga Ha'apai (HTHH) significantly impacted the Kingdom of Tonga as well as the wider Pacific region. The eruption column attained a maximum height of 58 km whilst the umbrella cloud reached a diameter approaching 600 km within about 3 hours. The intensity of volcanic lightning generated during the eruption was also unprecedented, with the Vaisala Global Lightning Database (GLD360) recording over 3 $\times 10^5$ strikes over a two-hour period. We have combined Himawari-8 satellite imagery with the spatiotemporal distribution of lightning strikes to constrain the dynamics of umbrella spreading. Lightning was initially concentrated directly above HTHH, with an areal extent that grew with the observed eruption cloud. However, about 20 minutes after the eruption onset, radial structure appeared in the lightning spatial distribution, with strikes clustered both directly above HTHH and in an annulus of radius ~ 50 km. Comparison with satellite imagery shows that this annulus coincided with the umbrella cloud front. The lightning annulus and umbrella front grew synchronously to a radius of ~ 150 km before the umbrella cloud growth rate decreased whilst the annulus itself contracted to a smaller radius of about 50 km again. We interpret that the lightning annulus resulted from an enhanced rate of particle collisions and subsequent triboelectrification due to enhanced vorticity in the umbrella cloud head. Our results demonstrate that volcanic lightning observations can provide insights into the internal dynamics of umbrella clouds and should motivate more quantitative models of umbrella spreading.

## Keywords

Hunga Tonga-Hunga Ha'apai, volcanic lightning, satellite, umbrella cloud

## Statements and Declarations

The authors declare that they have no competing interests.

This manuscript is a non-peer reviewed pre-print that has been submitted for publication in Bulletin of Volcanology. Supplementary Data can be accessed at https://doi.org/10.5281/zenodo.8011902.

## 1. Introduction

The 15 January 2022 eruption of Hunga Tonga-Hunga Ha'apai (HTHH) was hugely impactful for the Kingdom of Tonga and beyond, as well as being unique in the time of human observations for the scale of various associated physical phenomena. The eruption generated a tsunami (Gusman et al. 2022.; Omira et al. 2022), tragically causing loss of life and substantial damage (estimated at ∼ 90M USD) in Tonga (World Bank Group 2022), as well as causing a variety of impacts for the wider Pacific region (Global Volcanism Program 2022). Furthermore, the eruption plume reached a maximum height of ∼ 58 km (Carr et al. 2022; Proud et al. 2022), with ashfall from the associated umbrella cloud covering the Tongan islands (World Bank Group 2022; UNOSAT 2022). Aside from the unprecedented (in the satellite-observation era) height of the eruption column, the eruption was also remarkable for the atmospheric disturbances it created, with acoustic booms heard as far away as New Zealand and even Alaska (Global Volcanism Program 2022), an atmospheric Lamb wave observed to propagate across the globe (Amores et al. 2022; Matoza et al. 2022; Otsuka 2022; Wright et al. 2022; Vergoz et al. 2022; Yuen et al. 2022), as well as packets of gravity waves (Liu et al. 2022; Vergoz et al. 2022; Wright et al. 2022). These facts demonstrate the incredible power of the eruption, as well as bring to the fore the vulnerability of communities to natural hazards.

The edifice of HTHH is a mostly-submerged caldera on the Tonga-Kermadec Arc (Figure 1). Two islands, Hunga Tonga and Hunga-Ha'apai, represented the only parts of the caldera rim which were exposed subaerially (Bryan et al. 1972). Surtseyan style eruptions occurred in 2009 and 2014-2015 (Cronin et al. 2017; Colombier et al. 2018), with the latter eruption forming a new tephra cone which, following subsequent remobilisation, connected the two islands (Cronin et al. 2017; Garvin et al. 2018). Field observations of ignimbrites preserved on the two islands demonstrate that repeated caldera-forming eruptions have occurred, with the most recent between 1040 and 1180 CE (Cronin et al. 2017; Brenna et al. 2022). On 20 December 2021 a new eruptive phase initiated, with Surtseyan-style activity, seemingly similar to that observed in both 2009 and 2014-2015 (Gupta et al. 2022; Yuen et al. 2022). This eruption sequence continued intermittently until a larger eruption occurred on 13 January 2022 (UTC - the eruption was 14 January local time), producing an ash plume up to ∼ 18 km (Gupta et al. 2022). Notably, after this large eruption, high-resolution satellite imagery showed that much of the 2014-2015 cone material had been removed, with the islands of Hunga Tonga and Hunga Ha'apai now appearing separate (Yuen et al. 2022). The eruption episode seemingly ended with the climactic 15 January eruption a few hours later.

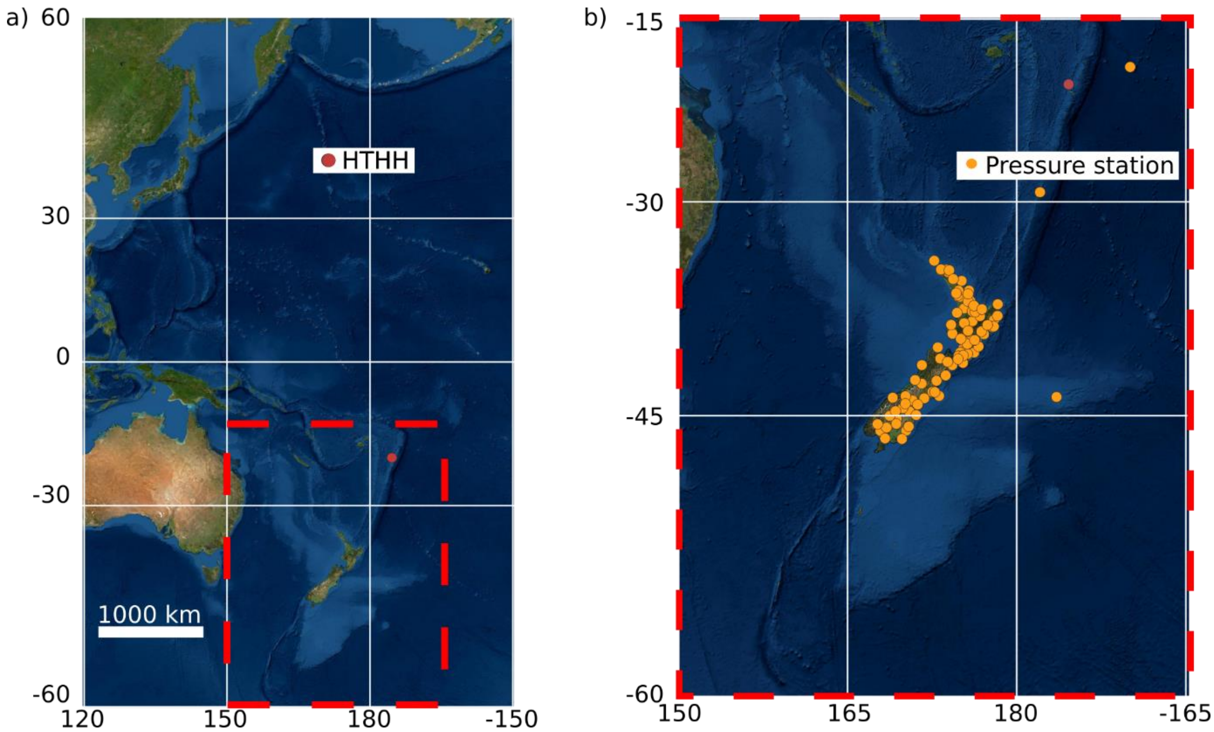


**Fig 1** a) Map of the west Pacific region showing the location of Hunga Tonga-Hunga Ha'apai (HTHH) (red circle). The region demarked by red dashed-lines shows the area shown in b) where the locations of the weather stations (orange circles) recording barometric pressure are shown (adapted from Gusman et al. (2022))

The remoteness of HTHH means that it is difficult to characterise eruptions through common field techniques. Eruptions at accessible volcanoes can be characterised through visible or infrared imagery (Self et al. 1979; Patrick 2007; Tournigand et al. 2017; Bombrun et al. 2018), proximal seismoacoustic observations (Jolly et al. 2017) and radar (Freret-Lorgeril et al. 2018) and lidar (Scollo et al. 2012) techniques. Additionally, eruption products and deposits can be rapidly characterised through sampling (Diaz Vecino et al. 2022), field observations (Bonadonna et al. 2011; Freret-Lorgeril et al. 2022) and petrological analysis (Pankhurst et al. 2022). Conversely, rapid observations of eruptions from volcanoes such as HTHH rely on far-field remote sensing techniques (McKee et al. 2021a, b). Satellite imagery, using a range of wavelengths, can provide a wealth of information on plume height and umbrella cloud extent (Prata et al. 2020; Corradini et al. 2020), whilst large eruptions can be observed using international acoustic sensors (Fee et al. 2010; Matoza et al. 2011) and teleseismic stations (Haney et al. 2017; Poli and Shaprio 2022).

At the time of writing, various studies have already utilised a number of these techniques to study the HTHH eruption and the associated phenomena. Seismoacoustic studies (Matoza et al. 2022; Poli and Shaprio 2022) have shown that the climactic eruption started in the 30 minutes prior to the largest seismoacoustic event of the sequence at 04:15 UTC and continued for approximately two hours. By tracking the Lamb wave signal across barometric (Gusman et al. 2022.; Wright et al. 2022) and infrasonic (Matoza et al. 2022; Vergoz et al. 2022) stations and through satellite imagery (Otsuka 2022), the peak disturbance can be shown to have an origin time of 04:29 - 04:30, with propagation speed estimates between 310 and 319 m s−1. From satellites, stereo methods have been used to determine a maximum plume height of 55 (Carr et al. 2022) to 58 (Proud et al. 2022) km, whilst showing a two-layer umbrella cloud, with lateral spreading at approximate altitudes of 20 and 34 km (Proud et al. 2022). Gupta et al. (2022) attempted to fit the umbrella radius $r_c$ as a function of time $t$ to a commonly used power law $r_c \sim t^{2/3}$ (Woods and Kienle, 1994; Costa et al. 2013; Mastin & Van Eaton 2022; Prata et al. 2020) but noted that the quality of fit was poor. Other studies have focused on the associated tsunami (Carvajal et al. 2022; Gusman et al. 2022.; Omira et al. 2022; Schnepf et al. 2022), atmospheric gravity waves (Liu et al. 2022), radiative impacts on the Earth's atmosphere (Sellitto et al. 2022) and the SO2 emissions associated with the eruption (Carn et al. 2022).

In addition to the above remote techniques, electromagnetic (EM) radiation generated by volcanic lightning has become a further source of information on explosive eruptions in recent years (Cimarelli and Genareau, 2022). Although a long-observed phenomena (Mather & Harrison 2006), the precise origins of volcanic lightning remain elusive. However, it is known that volcanic ash can retain a charge (Gilbert et al. 1991), possibly originating from fragmentation of the magma (fractoelectrification) (James et al. 2000), or particle-particle collisions (tribo-electrification) (Cimarelli et al. 2014). Whilst this charge may be important for aggregation of volcanic ash (Schumacher 1994; James et al. 2003; Pollastri et al. 2021), it is also likely to contribute to the development of charge separations required for lightning strikes (Smith et al. 2021). Nonetheless, tall and wet plumes seem to be associated with more intense lightning events (McNutt & Thomas 2015), suggesting ice precipitation is a dominant control on lightning occurrence (Prata et al. 2020; Van Eaton et al. 2020, 2022). In recent years, various studies have used lightning strikes detections, which are based on radiowaves, to observe the temporal evolution of lightning intensity during eruptions, in an attempt to relate these time series to eruption dynamics (Behnke et al. 2013; Van Eaton et al. 2016; Behnke et al. 2018; Prata et al. 2020; Van Eaton et al. 2020; McKee et al. 2021a, b; Van Eaton et al. 2022). These studies demonstrate that the EM radiation generated by volcanic lightning can provide crucial information on eruption processes. Additionally, broadband EM signals have also been used to investigate low-intensity volcanic lightning during Vulcanian eruptions at Sakurajima volcano, Japan (Aizawa et al. 2010, 2016; Cimarelli et al. 2016). Despite the rapid progress in recent years, quantitatively relating the properties of volcanic lightning to eruption dynamics has been difficult (Cimarelli and Genareau 2022), although Prata et al. (2020) demonstrated a correlation between plume height and the rate of lightning strikes during the 2018 eruption of Anak Krakatau.

In this paper, we study the HTHH eruption through 1) lightning strike timing and locations from the Vaisala Global Lightning Database GLD360, 2) observations of the air pressure perturbation due to the Lamb wave as it passed over New Zealand and 3) imagery of the eruption captured by the Himawari-8 satellite. By combining the spatiotemporal distribution of the lightning locations, together with satellite imagery, we provide insights into the dynamics of umbrella spreading and the internal distribution of vorticity and particle concentration. Additionally, integrating these observations with published teleseismic and infrasonic datasets (Matoza et al. 2022; Poli and Shaprio 2022) allows us to impose some constraints on the timeline of the eruption. Our results therefore have implications for the source conditions of both ashfall and tsunami models, and thus for assessing the impact of both this eruption and potential future activity.

## 2. Methods

### *2.1 Volcanic lightning*

We used lightning strikes recorded in the Vaisala Global Lightning Dataset GLD360, which includes the horizontal location (latitude and longitude) and timing of detected lightning strikes. For some of our analysis, we have reported the distance at which individual strikes have occurred from HTHH. Defining $\varphi_i$ and $\theta_i$ as the latitude and longitude of a given lightning strike, and $\varphi_H = -20.536°$ and $\theta_H = -175.382°$ the corresponding coordinates for HTHH (Global Volcanism Program 2022), the distance of the strike location from HTHH can be expressed as (Inman 1838)

$$d = 2R \sin^{-1}\left(\sqrt{H(\varphi_H, \varphi_i, \theta_H, \theta_i)}\right), \tag{1}$$

where

$$H(\phi_H, \phi_i, \theta_H, \theta_i) = \sqrt{\sin^2\left(\frac{\varphi_i - \varphi_H}{2}\right) + \left[1 - \sin^2\left(\frac{\varphi_i - \varphi_H}{2}\right) - \sin^2\left(\frac{\varphi_i + \varphi_H}{2}\right)\right]\sin^2\left(\frac{\theta_i - \theta_H}{2}\right)}, \tag{2}$$

and $R$ = 6378.1347 km is the Earth's radius (assuming a spherical Earth).

### *2.2 Barometric observations*

Ground level barometric pressure measurements were recorded from 92 New Zealand MetService weather stations (Figure 1b) at 1-minute intervals using Vaisala pressure sensors. Thus, a time series of pressure $P_i(t)$ was recorded at each station, where $i$ denotes the station label. The pressure time series, as well as the locations of all stations, have been included as Supporting Information files TableS1.csv and TableS2.csv, respectively This data has also been used to constrain properties of the barometric pressure disturbance which drove the meteotsunami associated with the eruption (Gusman et al. 2022). In order to better isolate the signal due to the HTHH eruption from long-period variations in $P_i(t)$, we filtered the data to produce a 60-minute moving average $\bar{P}_i(t)$ and finally calculated an adjusted pressure $P'_i(t) = P_i(t) - \bar{P}_i(t)$. From these time series $P'_i(t)$, we were able to identify the arrival time of the Lamb wave peak at each station from the maximum value of $P'_i(t)$ whilst also attempting to pick the time of the emergent Lamb wave onset. In order to track the propagation of the Lamb wave from HTHH, we calculated the distance of each station from the volcano using equation 1.

### *2.3 Satellite observations*

We use imagery from the 11.2 micron band of the Himawari-8 satellite to observe the volcanic plume and umbrella cloud associated with the eruption. Himawari-8 captures full-disk scans of the Earth's surface every 10 minutes, starting from the North Pole and in west-to-east stripes. Each image is timestamped with the moment the scan initiates whilst HTHH is observed 7 minutes after the start of the scan. Thus, an image timestamped at 04:00 UTC corresponds to an observation of HTHH at 04:07 UTC. We use these images to construct a general timeline of changes in plume and cloud features as well as follow the methodology of (Prata et al. 2020) to calculate the radial extent of the umbrella cloud in each image. This first involves contouring the brightness temperature (BT) at a threshold value, which was selected by visibly comparing the reproduced contour with the original image. We find that a threshold value of $T_{\mathrm{B,t}}$ = 250 K successfully produces a contour which visibly matches the edge of the umbrella cloud. We then remove any short wavelength noise from the image by applying a Gaussian filter with a standard deviation of 3 before producing a segmented image where pixels for which the BT $T_{\mathrm{B}} > T_{\mathrm{B,t}}$ are set to 1, with all other pixels set to zero. This effectively separates the volcanic cloud from the rest of the image but there are sometimes other, smaller objects also highlighted. We therefore remove all objects apart from the largest (which is invariably the plume) before filling holes in the remaining object. This is successful in producing a segmented image in which the plume is successfully isolated. We then extract the perimeter of this object as the desired contour.

In order to quantify the horizontal extent of the cloud, we wish to calculate the circular equivalent radius of this contour, which requires knowledge of the area inside the contour. To do this, we first project the latitude and longitude of each pixel on the contour onto a cartesian $x, y$ grid, with the origin located at an arbitrary point on the contour. We therefore calculate the east-west and north-south coordinates of each point using equation 1. Then, following (Prata et al. 2020), we calculate the area using Green's theorem

$$A = \iint_A \mathrm{d}x\,\mathrm{d}y = \oint_C x\,\mathrm{d}y, \tag{3}$$

where $C$ denotes the determined contour. The circular equivalent radius of the umbrella cloud is then calculated as

$$r_c = \sqrt{\frac{A}{\pi}}. \tag{4}$$

An implicit uncertainty in this method is that we are unable to quantify vertical variations in the lateral extent of the umbrella cloud meaning we cannot distinguish between spreading at multiple levels. The consequences of this shortcoming with be discussed in Section 4.

## 3. Results

### *3.1 Barometric data*

Figures 2a-e show examples of the high-pass filtered (see Section 2.2) barometric pressure signal received at some of the stations shown in Figure 1b. The precise locations of the stations can be found in the Supporting Information (Table S2.csv). The waveform received by all stations appears similar, with a characteristic N-shape. In all cases, there is a gradual increase in pressure over approximately 15 minutes, followed by a rarefaction before the signal restores. The total duration of the signal is approximately 1 hour. These observations are consistent with global observations of the Lamb wave produced by the eruption (Matoza et al. 2022; Wright et al. 2022).

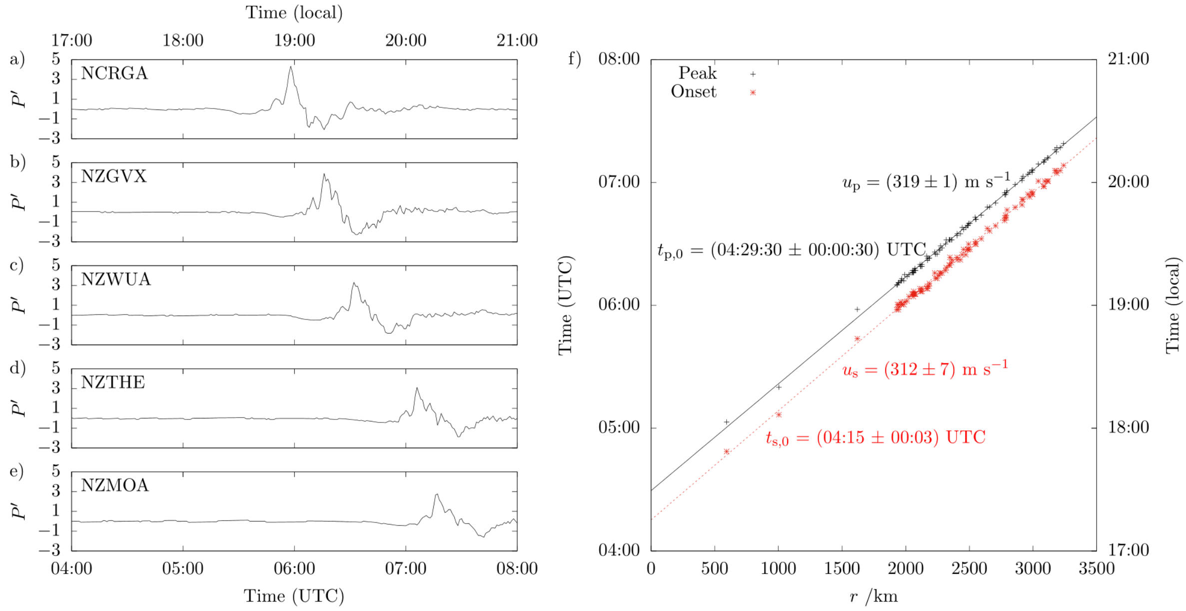


**Fig 2** a -e) Examples of the high-pass filtered barometric pressure time series recorded at some of the stations shown in Figure 1b. Locations of the stations can be found in the Supporting Information Table S2.csv. b) Arrival time of the peak (black crosses) and onset (red stars) of the barometric pressure disturbance associated with HTHH eruption. Straight lines (black solid and red dashed, respectively) show the linear fits. Raw data for peak arrivals also presented in Gusman et al. (2022)

From each weather station, we have identified the time for which $P'_i(t)$ is a maximum and plotted this as a function of distance from HTHH in Figure 2f in black. Additionally, we have attempted to select the arrival time of the onset of the disturbance although, given the arrivals are emergent, this is associated with a greater uncertainty. We see that the disturbance has propagated at an approximately linear velocity, with a linear fitting to the peak pressure disturbance obtaining $u_\mathrm{p}$ = 319 ± 1 m s$^{-1}$. When performing a linear fit to the arrival times of the onset of the disturbance, we obtain a slightly lower value of $u_\mathrm{s}$ = 312 ± 7 m s$^{-1}$. The discrepancy and larger uncertainty are likely due to the greater uncertainty associated with picking the arrival of the onset rather than the peak. We also extrapolate these linear relationships back to HTHH and obtain an origin time of the peak of $t_{\mathrm{p},0}$ = 04:29:30 ± 00:00:30 UTC and of the onset as $t_{\mathrm{s},0}$ = 04:15 ± 00:03 UTC. We must treat these origin times with caution though, as we are assuming that the near-field Lamb wave propagates at the same horizontal velocity as in the far field.

### *3.2 Satellite observations*

Video S1 in the Supporting Information shows a sequence of images captured by Himawari-8 in the 11.2 μm band showing the eruption of 13-14 January. The eruption plume first appears at 15:27 UTC, indicating an eruption start time between then and 15:17. The plume and umbrella cloud grow relatively axisymmetrically for about 3 hours, during which time faint concentric ripples in the umbrella cloud can be seen. After this, the cloud margins become diffuse whilst the cloud becomes stretched in an east-west orientation. Despite this, disturbances to the cloud above the vent can be seen to continue until about 12:00 UTC (14 January) indicating ongoing convection above the vent.

Figure 3 shows a sequence of images captured by Himawari-8 in the 11.2 μm band showing the main eruption on 15 January whilst Video S2 in the Supporting Information shows the same images as a video at higher spatial resolution and for a longer time period. At 04:07, no plume can be seen in the image, although closer inspection of the visible bands suggests a small plume may be evident. A plume becomes visible by 04:17 which rapidly expands until about 04:57.

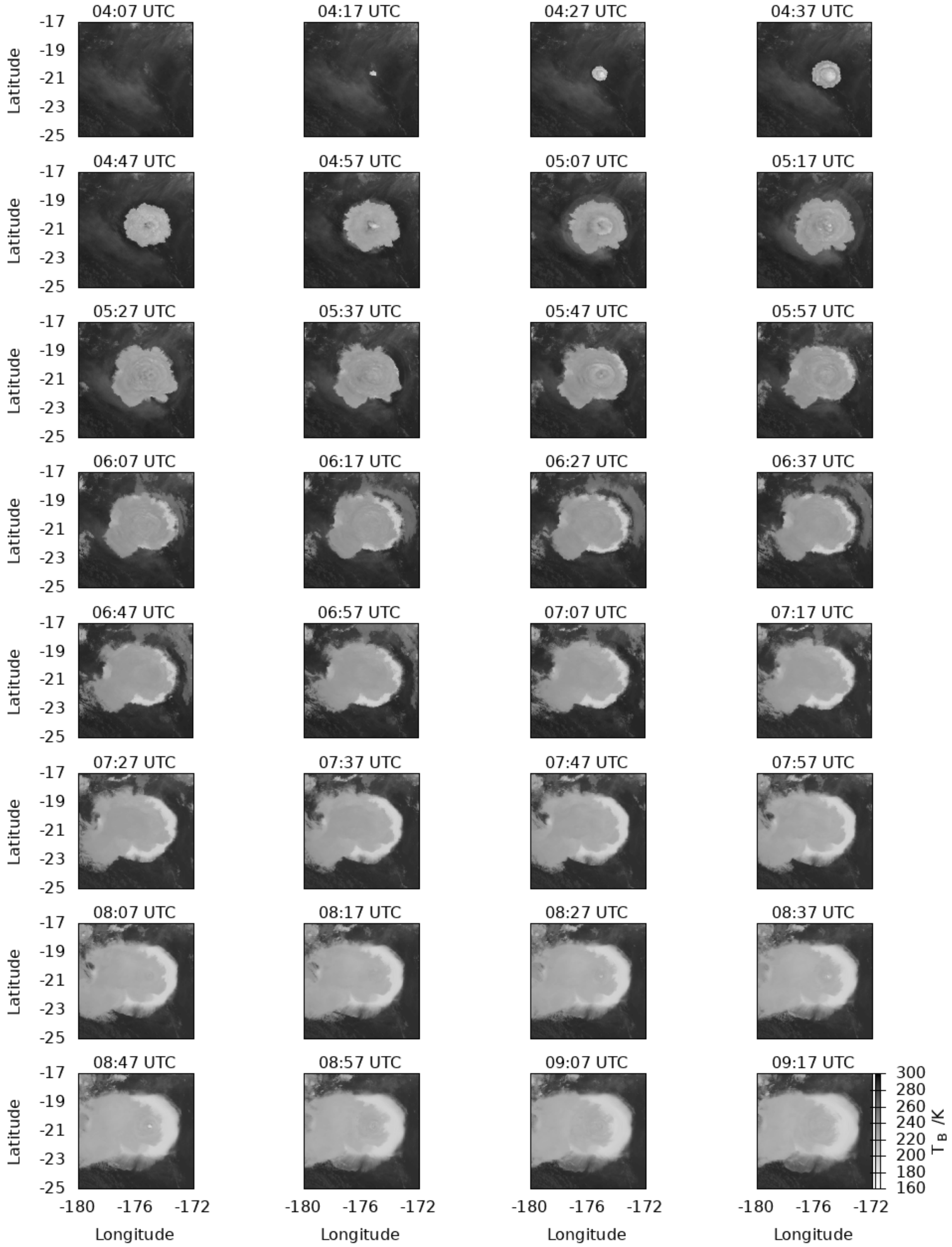


**Fig 3** Sequence of Himawari-8 images in the 11.2 micron band showing the evolution of the eruption cloud on 15 January

Beyond 04:57, the rate of expansion begins to slow whilst at approximately this time, a circular region of higher brightness temperature $T_B$ is seen to expand away from the cloud, remaining visible until about 05:37. Also at 05:37, it becomes possible to delimit vertical structure in the cloud. At the highest altitudes, there is a cloud of higher $T_B \approx 220 - 240$ K with a lower cloud with $T_B \approx 200 - 220$ K. From this time onwards, the upper cloud starts to drift to the west, while the lower cloud remains centred over HTHH, at least until the end of the dataset presented here (07:07). At 05:47, another wave-like disturbance in the brightness temperature is seen to propagate away from HTHH, at a faster velocity than the cloud propagation. It is particularly prominent to the north-east, and remains visible until 07:07. After this time, the upper umbrella cloud stops spreading radially and starts to drift towards the west, revealing more of the lower umbrella cloud, which continues to show concentric ripples on its upper surface. At 08:07, disturbances are again visible in the upper umbrella cloud above HTHH. These disturbances persist until approximately 09:07 but do not appear to result in any further radial spreading at the altitude of the upper cloud. Throughout the observation period, ripple-like structures can be observed in both the upper and umbrella clouds.

Figure 4 shows the umbrella cloud radius $r_c$ as a function of time for the time period shown in Figure 3. It can be seen that the cloud already has a radius of about 20 km by the time it is first seen at 04:17, which rapidly increases until about 180 km by 04:57. Following this, the spreading velocity drastically decreases, with the cloud reaching a radius of about 280 km by 07:07.

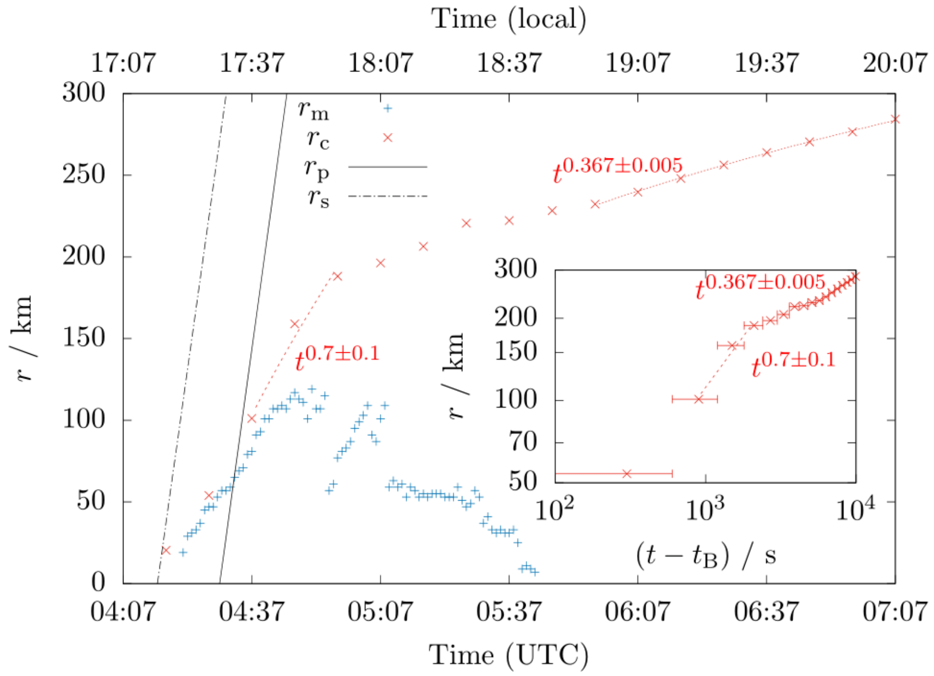


**Fig 4** Plot showing the radial position $r_c$ of the outer edge of the umbrella cloud (red crosses), the modal radius of lightning strikes $r_m$ (blue crosses) and the extrapolated position of the peak $r_p$ and onset $r_s$ of the Lamb wave (solid and dashed black lines, respectively) as functions of time. The dashed and dotted red lines show power-law fits to the umbrella cloud radius as a function of time between 04:37 and 04:57 and 05:57 and 07:07, respectively (all times UTC). The inset shows $r_c$ as a function of $(t - t_B)$, where $t_B$ is defined as the time at which gravitational spreading of the umbrella begins, taken here to be at 04:22 ± 00:05. The horizontal error bars correspond to this uncertainty on $t_B$

Some previous studies have attempted to quantify cloud spreading by fitting $r_c(t)$ with a power law of the form $r_c \sim t^{2/3}$ (Costa et al. 2013; Mastin and Van Eaton 2022; Carn et al.

2022; Gupta et al. 2022). However, Figure 4 clearly shows that a single power law will be insufficient to describe the data. Instead, following the results of Pouget et al. (2016), we fit separate power laws to different portions of the dataset, recognising that cloud spreading can transition between different regimes. First, we need to define a time $t_{\mathrm{B}}$ at which gravitational spreading begins. This is difficult to identify, particularly given that satellite retrievals only have a 10-minute period. At 04:17, satellite imagery (Figure 3 and Video S1) shows that the plume has a "mushroom shape" whereas by 04:27, a flatter, outer region has started to spread, presumably through buoyancy. It seems reasonable to assume that buoyant spreading began during this interval so, thus, we assign $t_{\mathrm{B}}$ = 04:22 ± 00:05. Next, we visually inspect $r_{\mathrm{c}}(t - t_B)$ on log-log axes (inset of Figure 4). It can clearly be seen at late times, the data converges towards a straight line, indicating an asymptotic power-law relationship. At early times, such behaviour is much harder to identify owing to both the low temporal resolution of the data and uncertainty on the appropriate value of $t_{\mathrm{B}}$. However, we note a possible power-law trend for the first four data points, followed by a transitional period to the late asymptotic regime. Motivated by these semi-quantitative observations, we therefore fit power-law relationships for the two time periods from 04:37 to 04:57 and from 05:57 to 07:07, obtaining $r_{\mathrm{c}} \sim t^{0.65 \pm 0.04}$ for early times and $r_{\mathrm{c}} \sim t^{0.367 \pm 0.005}$ at late times. We choose not to include the data point at 04:27 in the fitting owing to the large effect of the uncertainty on $t_{\mathrm{B}}$ at this early time.

### *3.3 Lightning location data*

In Figure 5a, we present the number of lightning strikes per minute $n$ that occurred in the 48 hours starting from 11:00 UTC on 13 January. Consequently, this time period covers both the eruption of the 13-14 January, as well as the climactic event on 15 January. Both events are clearly distinguished in the dataset. Lightning associated with the first eruption commenced around 16:00 on January 13 and continued until about 12:30 the following day, with a peak intensity of about 1000 strikes per minute around one hour into the eruption. This was followed by a hiatus of about 18 hours, with small bursts of lightning at 14:07-14:42, 15:44-15:54 and 18:17-18:32, until the onset of the climactic eruption the next day, shown in more detail in Figure 5b. Here we see a rapid increase in lightning intensity, starting at 04:11 and increasing to a peak of $n \approx 5 \times 10^3$ at 05:03. This increase is punctuated with local maxima occurring at 04:18, 04:34 and 04:50. Following this peak, $n$ decays, again in a spiked fashion, with a particularly prominent peak at 05:47, until lightning almost ceases at about 07:15, with only occasional lightning strikes occurring. Lightning recommences again shortly before 08:00, again showing a punctuated increase in $n$ until a peak of $n \approx 1500$ at around 08:48 before rapidly falling away. A final increase in $n$, for about 1 hour, occurs around 09:30.

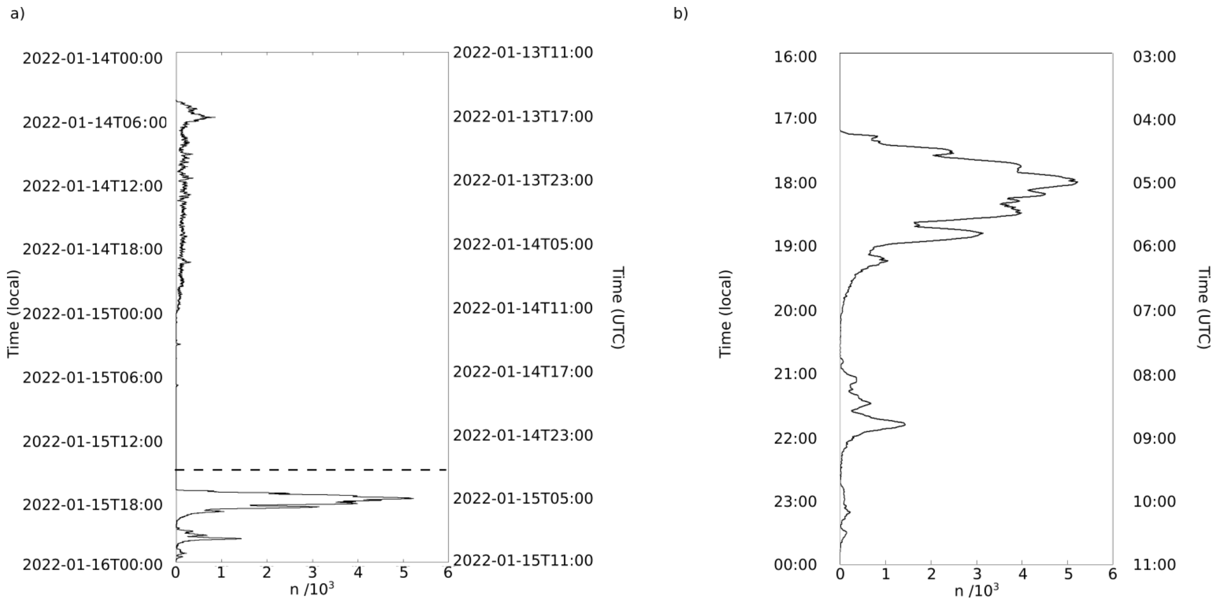


**Fig 5** a) The number of detected lightning strikes from GLD360 per minute $n$ for the 48 hours from 11:00 UTC January 13th. The period later than the dashed line at 03:00 UTC January 15$^{\text{th}}$ is shown in b)

Whilst the time series shown in in Figure 5 demonstrate the temporal variation in $n$, the Vaisala data also contains useful information concerning the spatial distribution of the lightning strikes. Video S3 shows lightning strike locations overlain on satellite imagery for the 13-14 January eruption. In each frame, we show the locations of strikes occurring in the minute bracketing the time of satellite image acquisition, i.e., at 04:17, we show strikes occurring between 04:16:30 and 04:17:30. It should be noted that the video shows an apparent spatial offset between the lightning locations and the eruption cloud. This is due to a parallax effect associated with the satellite imagery (Bielinski 2020) (see Appendix A).

In Video S3, we see that during the eruption of 13-14 January, lightning strikes occurred directly above HTHH from the onset of the eruption at about 15:17 and persisted continuously until about 11:47 the following day. After this time, lightning generation becomes sporadic, and appears to coincide with the appearance of discrete eruption plumes at 12:27, 14:07 and 15:47. This pattern is consistent with the time series of lightning strikes presented in Figure 5a. It is also notable that, despite the umbrella cloud spreading to diameters of a couple hundred km, the lightning remains focused in a much smaller region directly above the vent.

In Figure 6, we show the locations of strikes during the main eruption of January 15. The same data are also presented in Video S4 of the Supporting Information. Here, in order to enable a comparison between the location of the umbrella cloud and the spatial lightning distribution, we have corrected for the satellite parallax effect noted above. To do so, we have isolated the volcanic cloud using the $T_{\mathrm{B}}$ = 250 K contour, as described in Section 2.3. Then, we relocate each pixel inside this contour using the parallax projection method described in Appendix A. This correction relies on knowing the altitude of the umbrella cloud. To estimate this, we took the time series of altitudes determined by Proud et al. (2022). Whilst this is a strong assumption, both Figure 6 and Video S4 show there is good spatial agreement between the lightning strikes and the un-projected umbrella cloud.

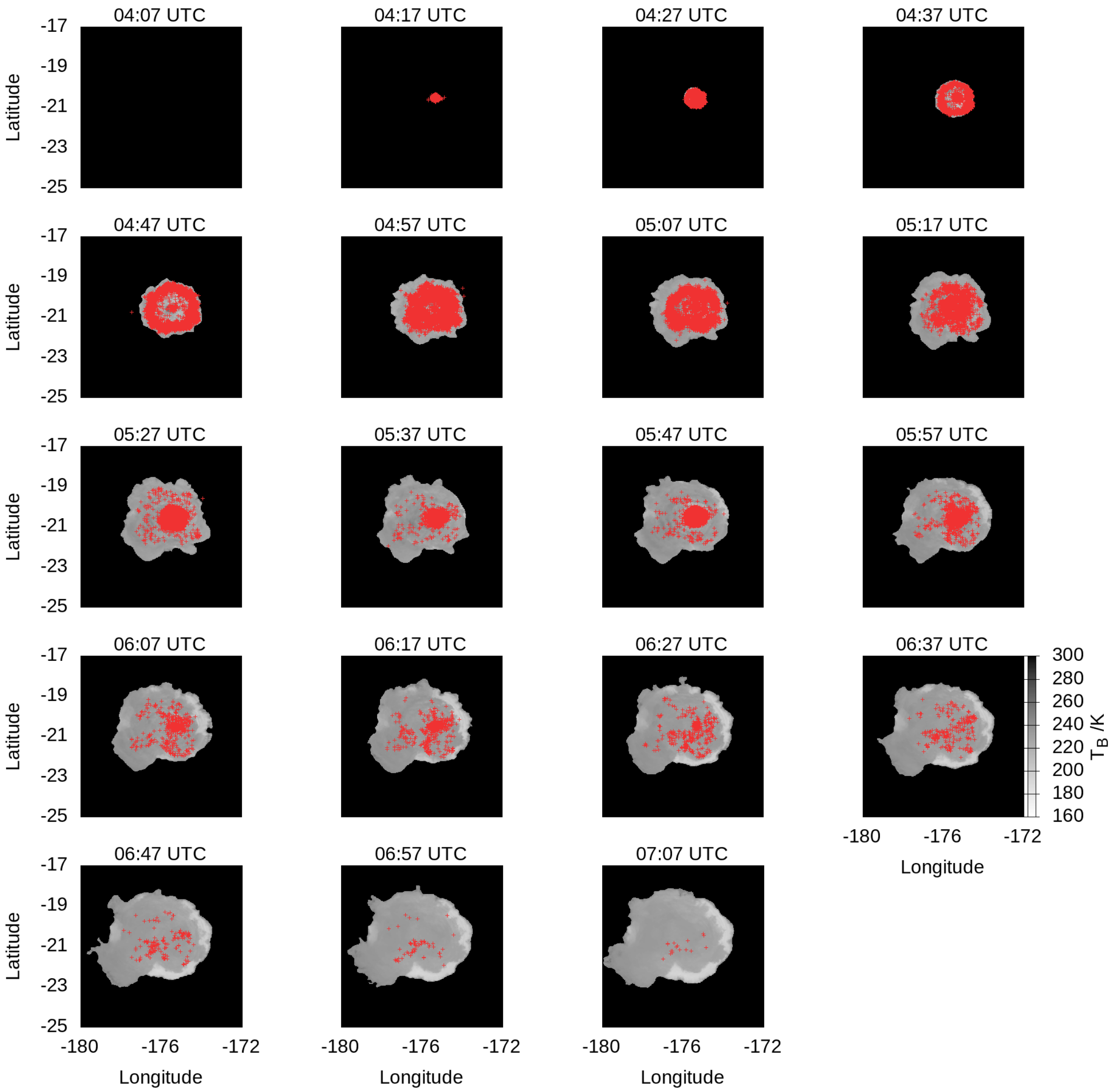


**Fig 6** Sequence of Himawari-8 images in the 11.2 micron band showing the evolution of the eruption cloud. Overlain in red are Vaisala lightning data locations recorded in the 1-minute window which brackets the image acquisition time. The cloud has been isolated from the image and its position corrected for parallax (see Appendix A)

Initially, the areal extent of the lightning matches that of the umbrella cloud. However, by 04:27, we see that radial structure has appeared in the spatial distribution of the lightning, with strikes clustered both directly above HTHH and in an annulus at a larger diameter. This annulus expands until about 04:47, with only occasional strikes occurring between the annulus and the central cluster above HTHH. By 04:57, the intensity of lightning in the annulus has started to decrease, but radial structure can still be made out, with lightning focused at a smaller radius. Radial structure appears to persist until about 05:37, but there appears to be variability in the radial locations at which lightning is focused during this time.

From 05:37 onwards, lightning remains focused at smaller radii, decreasing in intensity across the umbrella cloud. Beyond 07:07, we no longer have information on the altitude of the cloud, so do not consider the comparison between the unprojected satellite imagery and the spatial distribution of the lightning strikes further.

In Video S5 of the Supporting Information, we again present the lightning spatial distribution of the 15 January eruption but at a higher temporal resolution, showing the lightning strikes that occur every minute between 04:00 and 11:00. At this greater resolution, it can be seen that once the initial lightning annulus stops expanding at 04:47, a second ring of lightning detaches from this annulus and propagates back towards the vent. The large number of lightning strikes in the area means it is difficult to fully distinguish, but this secondary annulus becomes particularly prominent at 04:56-57 and persists until around 05:29, at which point it becomes indistinguishable from lightning above the vent.

In order to quantify the spatial distribution, as well as the propagation of the initial lightning annulus, we bin the lightning strikes into 2 km radial bins around HTHH. Figure 7 shows subsequent histograms of the number of strikes $n'$ for selected one-minute intervals. Additionally, Video S6 in the Supporting Information shows the same histograms but for every minute from 04:00 to 07:00. At 04:09 UTC, there are just two lightning strikes, centred directly above HTHH. At 04:17, lightning is distributed across a circle centred on HTHH with a radius of about 34 km and a decreasing density with $r$. However, by 04:23, the lightning has become more evenly spread, out to a diameter of about 50 km, with a slight peak at $r$ = 32 – 34 km. This peak then becomes more pronounced and propagates outwards until about 04:47, at which point it has reached approximately 118 km. During this time, most of the lightning is concentrated in this annulus, with a smaller amount occurring within the first 20 km from HTHH and much less lightning at intermediate distances.

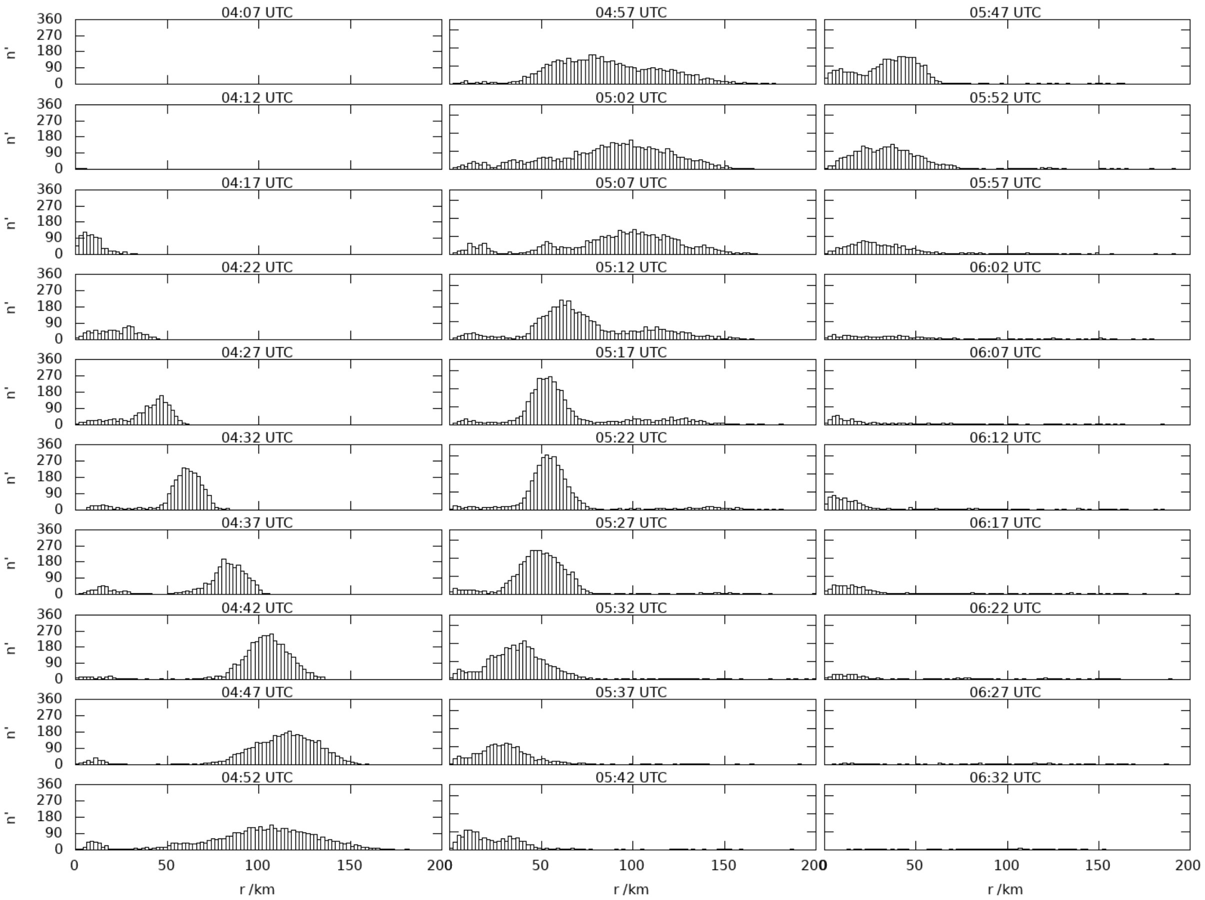


**Fig 7** Histograms showing the radial distribution of lightning during the climactic eruption. *n* is the number of lightning strikes in a 2 km radial bin and *r* is the distance from HTHH

In order to track the location of the lightning annulus, we define $r_{\mathrm{m}}(t)$ as the modal radius (corresponding to the maximum of $n'$) of the histograms in Figure 7. In Figure 4 we see that $r_{\mathrm{m}}$ initially trends similarly to $r_{\mathrm{c}}$. Beyond 04:47, temporal variations in the histograms in Figure 7 become noisy, but it is possible to discern the inward propagating annulus as a peak in $n$ at $r \approx 50$ km. This peak first appears at about 04:53 but becomes particularly prominent from about 05:09 until 05:30, at which time it starts to merge with the lightning directly above the vent. From this point onwards, $n'$ decreases with $r$ until just after 06:30, as the total number of lightning strikes decreases and the lighting becomes uniformly distributed across the umbrella cloud.

## 4. Discussion

The detected lightning locations, together with the barometric pressure and infrared satellite observations, allow us to place some constraints on the timeline of events at HTHH. We also use teleseismic (Poli and Shaprio 2022) and infrasound (Matoza et al. 2022) data, as well as satellite-derived plume height estimates (Carr et al. 2022; Proud et al. 2022) published elsewhere to support our interpretations. A critical part of this analysis concerns the rate of spreading of the umbrella cloud and primary lightning annulus (Figure 4). We therefore first discuss the implications of our results for the dynamics of umbrella cloud spreading (Section 4.1), before presenting an eruption timeline (Section 4.2).

*4.1 Umbrella cloud spreading*

### 4.1.1 Satellite observation

The lightning strike locations (Figures 6 and 7) and the satellite imagery (Figure 3) have allowed us to develop a description of how the umbrella cloud spread. Figure 4 shows that the early spreading appears to follow a power law $r_c \sim t^{0.7\pm0.1}$. Although this is consistent with the commonly-used theoretical scaling $r_c \sim t^{2/3}$ (Woods and Kienle 1994; Costa et al. 2013; Mastin and Van Eaton, 2022), there is significant uncertainty on our result owing to uncertainty on the choice of $t_B$. Additionally, Johnson et al. (2015) showed that shallow water models for spreading of a continuously-fed instrusion resisted by inertial drag fail to permit this scaling law and instead found $r_c \sim t^{3/4}$, again within uncertainty of our result. Our results thus highlight that the temporal resolution of satellite retrievals mean satellite imagery alone cannot be used to distinguish between these spreading models, for this early growth.

As spreading continues, $r_c(t)$ passes through a transitional regime between 04:57 and 05:37, after which a new asymptotic regime with $r_c \sim t^{0.352\pm0.005}$ ensues. Since now $t \gg t_B$, uncertainty on $t_B$ has much less impact on the fitted value of the exponent. The obtained fitting is close to the prediction of $r_c \sim t^{1/3}$ from the single-layer shallow water model of Ungarish and Zemach (2007) for the spreading rate of an instantaneously-fed intrusion resisted by inertial drag. Thus, it appears that, during the transitional regime, the supply of material to the umbrella cloud ceases. However, our lightning location (Figure 7) as well as seismic data (Matoza et al. 2022; Poli and Shaprio 2022) suggest extrusion at the vent may have continued until shortly after 06:00. One possible explanation is that the MER of the climactic event decreased after approximately 05:00, with the newly-erupted material unable to contribute to the outward spreading of the cloud. Another possibility is that an increasing amount of water became entrained into the eruptive column, leading to further collapse of the vertical plume, preventing eruptive material entering the umbrella cloud (Koyaguchi and Woods 1996; Prata et al. 2020).

### 4.1.2. Spatiotemporal distribution of lightning

More detail to this picture can be provided by the spatiotemporal distribution of lightning (Figures 6 and 7). Particularly pertinent is the primary lightning annulus which spreads radially outwards from 04:27 until about 04:47. Assuming lightning is produced due to particle collisions leading to charge differences, we can use the spatial distribution of the lightning as a proxy for a map of where particle collisions occur. The coincidence of the annulus with the front of the umbrella cloud (Figure 4) suggests that an enhanced rate of particle collisions is taking place at the umbrella front. A possible explanation for this is the umbrella front is thicker than the inner region, thus enhancing the depth-integrated ash and ice concentration, another prediction from the same shallow water model which predicts the $t^{3/4}$ spreading rate (Johnson et al. 2015). Another possibility is that vorticity, rather than the particle concentration, is enhanced in the head, as has been seen in laboratory-scale axisymmetrically spreading gravity currents (Patterson et al. 2006; Yuan and Horner-Devine 2013). In these flows, the front of the current spreads as a turbulent vortex ring, with the interior of the flow spreading as a thinner, more laminar layer. This reduction in both flow depth and vorticity of the interior of the flow, i.e., away from the front, may lead to reduced rates of particle collisions in this region, explaining the lack of lightning generated behind the current front. This scenario is depicted in Figure 8a.

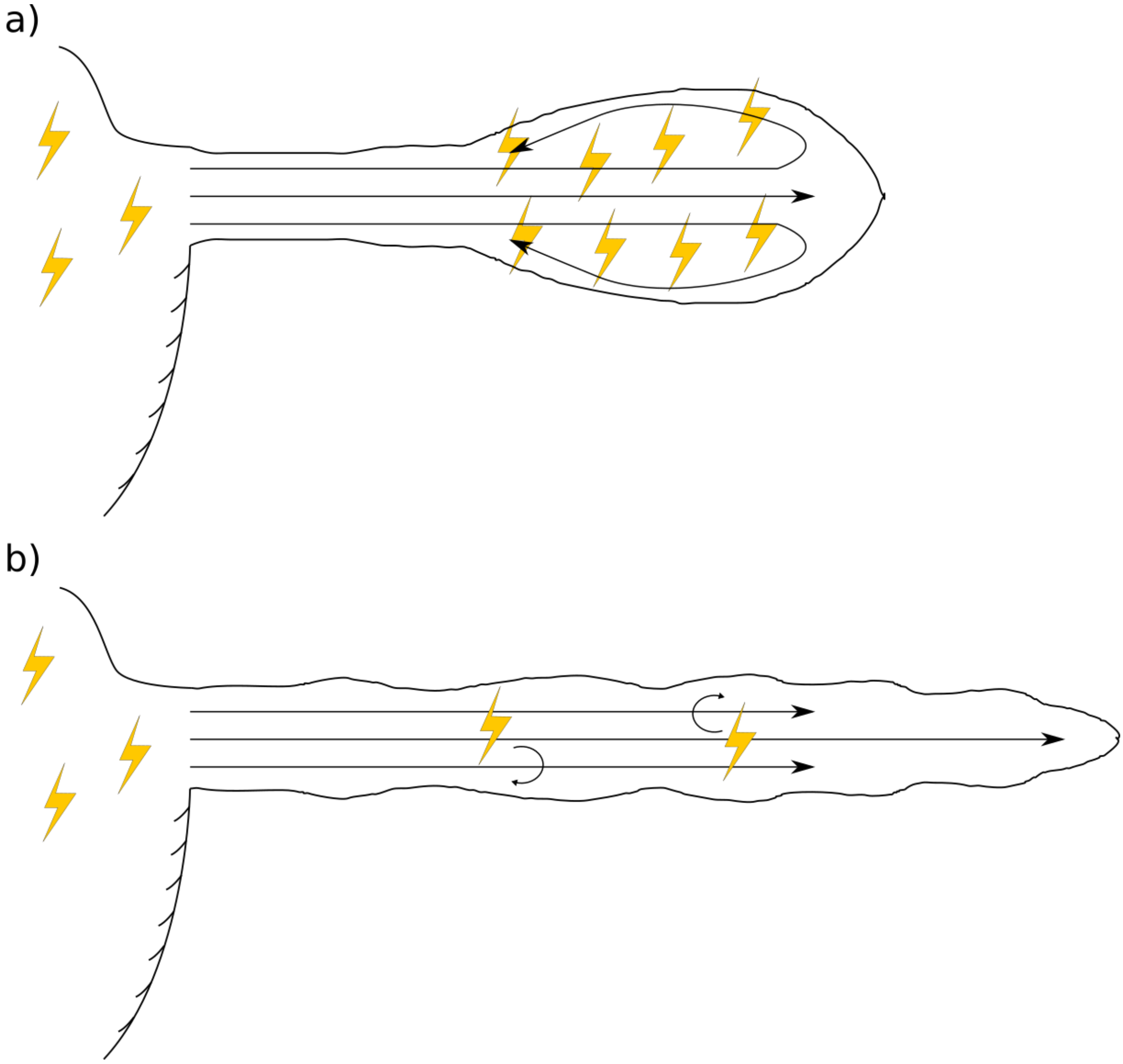


**Fig 8** Schematic depicting possible evolution of the umbrella cloud spreading. a) The initial buoyant spreading is sufficiently fast to generate a pair of vortex rings in a thickened head. The vorticity in this head is likely to lead to intense particle collisions, subsequent triboelectrification and discharges, resulting in the observed lightning annulus. b) At later-times, the vortex ring has decayed, resulting in a more laminar intrusion. There are fewer particle collisions and more uniform lightning

The lightning annulus appears to decay at approximately 04:47, with a secondary annulus detaching and propagating back towards the vent, whilst radial structure within about 75 km from the vent persists until about 05:30. Since we have no vertical information concerning the lightning strike locations, these later observations are difficult to decisively interpret. Experimental observations of axisymmetric gravity currents show that the vortex ring representing the current head can decay due to the presence of azimuthal instabilities at a critical radius $\sim 1.7r_0$, where $r_0$ is the initial radius of the current (Patterson et al. 2006). This would result in a more laminar umbrella cloud, such as that depicted in Figure 8b. We observe breakdown of the lightning radius at approximately r = 117 km. If we assume, as above, that gravitational spreading began between 04:17 and 04:27, then $r_0$ is between 20 and 54 km, respectively. Our lightning annulus therefore breaks down somewhere between r = $2.2r_0$ and $5.85r_0$, significantly greater than this critical value. However, given the large uncertainty on $r_0$, as well as in how the vorticity field evolution controls the lightning spatial distribution, it remains entirely possible that the primary lightning annulus decay represents the breakdown of this vortex ring.

Between 04:55 and 05:30, the secondary annulus seemingly contracts, moving back towards the vent. Whilst this is seemingly counter-intuitive, this does not necessarily correspond to the flow of material in the umbrella cloud back towards the vent. Indeed, using the same shallow water equations as Johnson et al. (2015), Ungarish et al. (2016) showed that, once an axisymmetric intrusion reaches a certain radius, the inner boundary of the thickened head can start moving back towards the centre of the intrusion. This inner boundary is likely to be a site of considerable vorticity and particle collisions. Consequently, the retreating lightning annulus may correspond to this behaviour. However, dedicated numerical modelling, using shallow-water models (Ungarish and Zemach 2007; Johnson et al. 2015; Ungarish et al. 2016) with suitable input parameters for the HTHH eruption, is necessary to test this.

### *4.2. Timeline of events at HTHH*

The eruption onset time remains an open question. Yuen et al. (2022) suggest that the climactic event initiated at 04:02 ± 00:01 UTC. However, the evidence supporting this is unclear. From our datasets, the earliest evidence we have for the climactic event occurring are the first two associated lightning strikes at 04:09 UTC (Videos S3, S4), followed by a rapid increase in $n$ starting at 04:12. Although it is not possible to resolve the altitude of lightning strikes, observations from other wet eruptions suggest the eruption plume needs to reach a sufficient altitude for ice formation to occur in order to trigger sufficient lightning once the plume mixture temperature drops below 20 ◦C (Van Eaton et al. 2020, 2022). Although the exact height at which this occurs will depend on the initial temperature of the eruptive material, the mass eruption rate (MER) and the vertical temperature profile of the atmosphere, lighting-associated wet plumes from Anak Krakatau in 2018 (Prata et al. 2020) and Taal in 2020 (Van Eaton et al. 2022) reached 8-10 km before lightning was detected. We therefore suggest that the plume top reached the level of ice nucleation when $n$ started rapidly increasing at 04:12 and the earlier lightning strikes are associated with charged ash particles (not ice) at lower altitudes. Without knowledge of the MER at eruption onset, it is difficult to estimate how fast the plume would have risen, and therefore the onset time of the eruption. However, since a plume is not seen in the infrared channel at 04:07 (Figure 5), it seems reasonable to suggest that the eruption initiated sometime between 04:07 and 04:09. This is consistent with seismic events at 04:06 and 04:07 detected on regional seismometers (Matoza et al. 2022).

Following the eruption onset, backwards extrapolation of the arrival times of the onset of the Lamb wave (Figure 2) suggest an origin time of 04:15 ± 00:03. Within uncertainty, this corresponds with the primary seismoacoustic event (moment magnitude 5.7 - 5.8) of the eruption which occurred at 04:14:45 (Matoza et al. 2022; Poli and Shaprio 2022). It seems likely this corresponds to the largest explosion of the sequence. This clearly very energetic explosion would have been associated with an extremely large MER, undoubtedly contributing to the large increase in values of $n$ at this time. This probably also led to an increase in the plume radius, leading to the almost step-like increase in the modal radius of the lightning strikes at around 04:20 (Figure 4). From this time onwards, the lightning annulus starts to spread.

Plume height retrievals from satellite imagery show the maximum plume height increased from about 22 km at 04:17 to 55 km at 04:37 (Carr et al. 2022; Proud et al. 2022), demonstrating that the release of material associated with the large explosion at 04:15 was sufficiently strong to generate a plume of unprecedented (in the satellite era) vertical scale. By 04:47, the same dataset shows that the top of the plume has collapsed, leaving what Proud et al. (2022) refer to as a “donut-shaped cloud”. This suggests there may have been a drop in the MER, meaning the height of the overshoot could not be sustained. Another possibility, as mentioned in Section 4.1 is column collapse. At the same time, the number of lightning strikes per minute directly above the vent has reduced from a maximum of about 130 at 04:17 until almost vanishing from 04:53-04:57. This also suggests that the rate of particle collisions in the central part of the eruptive column has reduced. However, Proud et al. (2022) also demonstrate that at 04:57, “tendrils” of plume material extend up to 58 km in altitude. These tendrils, however, are much narrower in extent than the initial overshooting dome, so may not contain enough particulate matter to leave a clear signature in the lightning data. Nonetheless, the peak in the total number of lightning strikes $n$ occurs shortly afterwards at 05:03. This suggests that HTHH continued to erupt material at a high rate, maintaining turbulent convection of the particle/ice-rich plume, after the initial strong explosions.

From the appearance of the lightning ring at 04:20, radial structure remains in the spatial distribution of the lightning pattern until about 06:00, nearly two hours after the eruption onset. As Figure 8 shows, the location of local maxima in $n$ during this time varies considerably. Whilst this undoubtably contains information on the time varying intensity of the eruption, an understanding of how this pattern depends on radial spreading of the umbrella cloud is likely necessary in order to fully develop these interpretations.

Final observations from the satellite imagery that may be used to infer eruption chronology are the wavelike disturbances in BT seen to propagate away from the umbrella cloud at 04:57 and 05:47 (Figure 3 and Video S1). These are likely to be gravity waves generated by events at HTHH (Vergoz et al. 2022; Wright et al. 2022). Since they only become visible once they have reached the edge of the umbrella cloud, which has a radius of approximately 180 and 220 km, respectively, their origin time at HTHH must be earlier than the time at which they become visible. Matoza et al. (2022) noted a significant infrasonic event with an origin time of 04:30 that might explain the earlier wave. This event was the most widely detected in their global infrasound network but seemingly had no seismic nor hydroacoustic signature. An explanation for this event remains to be uncovered.

## 5. Conclusions

We have used satellite observations, lightning strikes detections by the GLD360 network and barometric pressure measurements to study the 15 January 2022 HTHH eruption. Our results have enabled us to make interpretations concerning both the timeline of the eruption and also the spreading dynamics of the umbrella cloud. The climactic phase of the eruption initiated at approximately between 04:07 and 04:09 UTC. The eruption consisted of a series of explosions lasting until about 06:00 (Poli & Shapiro, 2022), with the largest explosion occurring at 04:14 ± 00:03. The volcanic plume was first seen by the Himawari-8 satellite at 04:17, and reached an altitude of 55 km by 04:37 (Carr et al. 2022; Proud et al. 2022). Throughout the eruption, there remains a focus of lightning strikes above the vent. However, from about 04:20, an annulus of lightning strikes is observed, expanding outwards from an initial radius of ~ 50 km to ~ 150 km by 04:47 (Figure 7). We definitively show that the expansion rate of this annulus is not linked to the propagation of the generated Lamb wave, which had a significantly faster celerity (Figure 4). Instead, we see that the annulus is coincident with the front of the expanding umbrella cloud (Figure 6). We thus suggest that, during this time, the umbrella front has a strong vortical structure, leading to frequent collisions and subsequent triboelectrification of the ash and ice particles present. The lightning annulus is observed to decay at about 04:47, seemingly contracting and becoming poorly-defined, although radial structure persists until about 05:37. This could be explained by decay of the vortex ring into a 3-dimensional turbulence field (Patterson et al. 2006) and the transition of the umbrella to a more laminar intrusion. Although the climactic eruption phase appears to end at about 06:00, a small uptick in the number of lightning strikes and observed disturbances in the umbrella top above HTHH suggest eruptive activity resumed at about 08:07, lasting for approximately one hour.

Our interpretations linking the spatiotemporal distribution of lightning strikes to the internal dynamics of umbrella spreading remain qualitative. Further testing of our proposed conceptual model requires a combination of numerical and experimental modelling. Shallow-water models, such as those by Johnson et al. (2015) and Ungarish and Zemach (2007) could be used to make predictions for the rate of spreading for the umbrella cloud and, possibly, for the observed contraction of the lightning annulus (Ungarish et al. 2016). However, this will require suitable input parameters for the HTHH eruption to be determined. The data presented here, along with insights on the eruption timeline and plume height from other studies (Carr et al. 2022; Matoza et al. 2022; Poli and Shapiro 2022; Proud et al. 2022) can provide a starting point for this. However, shallow-water models only make predictions for the mean horizontal flow fields in the intrusion and will be unable to resolve the vorticity that we hypothesise is essential for generating the lightning annulus. Thus, laboratory experiments, e.g., Patterson et al. (2006) and Yuan and Horner-Devine (2013), and fully resolved numerical simulations are also required.

**Acknowledgements**

The authors thank Chris Johnson for insightful discussions. Lightning location data was provided by Vaisala from their Global Lightning Dataset GLD360. This project was supported by the New Zealand Ministry of Business, Innovation and Employment (MBIE) through the Hazards and Risk Management programme (Strategic Science Investment Fund, contract C05X1702).

## Appendix A: Parallax correction

Objects at altitude above the Earth's surface appear at erroneous spatial locations when viewed by satellites due to a parallax projection (Figure A1). In the following, we use S to denote the location of satellite, P to denote the true location of an object at altitude and P′ the apparent projected location of P on the Earth's surface. The Earth itself is approximated as a sphere with a radius of $R$ = 6378.1 km. Since Himawari-8 is geostationary and HTHH is in the tropics, this is a reasonable assumption. We also use both spherical polar and Cartesian coordinate systems, before transforming to latitude and longitude coordinates at the end. The polar coordinate $\varphi$ is measured with respect to polar north, the azimuthal angle $\theta$ westward with respect to the prime meridian and the radial coordinate $r$ with respect to the Earth's centre. The corresponding Cartesian system is defined as

$$x = r \sin\varphi \cos\theta, \tag{A. 1}$$

$$y = r \sin\varphi \cos\theta, \tag{A. 2}$$

and

$$z = r \cos\varphi. \tag{A. 3}$$

Thus, in Cartesian coordinates, the position vector of S is given by

$$\boldsymbol{x}_{\mathrm{s}} = (r_{\mathrm{s}} \cos\theta_{\mathrm{s}}, r_{\mathrm{s}} \sin\theta_{\mathrm{s}}, 0) = (R + A)(\cos\theta_{\mathrm{s}}, \sin\theta_{s}, 0)\,, \tag{A. 4}$$

where $r_{\mathrm{s}} = R + A$ is the radial position of S, $A$ = 35793 km is the satellite altitude and $\theta_{\mathrm{s}}$ is the azimuthal position of S. Similarly, the position vector of S′ is given by

$$\boldsymbol{x}' = (r' \sin\varphi' \cos\theta', r' \sin\varphi' \cos\theta'\,, r' \cos\varphi') = R(\sin\varphi' \cos\theta', \sin\varphi' \cos\theta'\,, \cos\varphi'), \tag{A. 5}$$

where $r'$, $\varphi'$, $\theta$' are the radial, polar and azimuthal positions of P′, respectively.

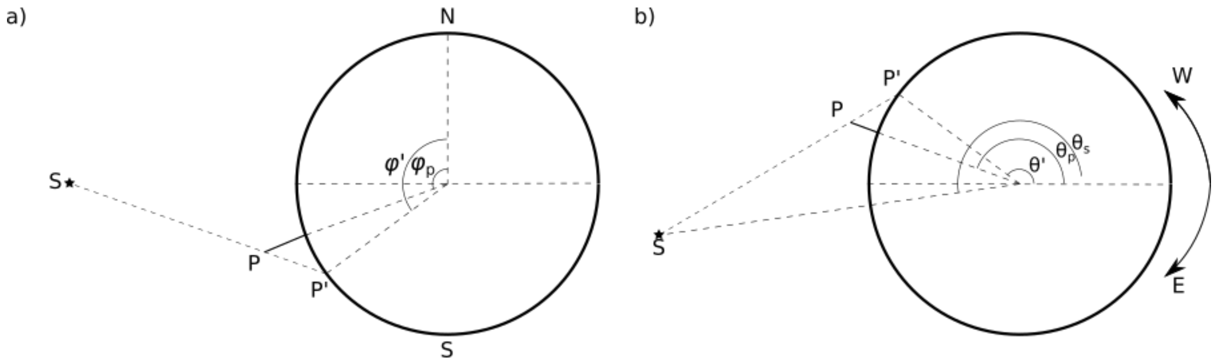


Figure A1. Schematic showing the geometry leading to the parallax effect with a) view showing the North (N) and South (S) poles and b) a cross-section through the Earth's equator, showing west (W) and east (E) directions. S denotes the location of the satellite, P the top location of the plume and P′ the projected location of the plume on the Earth's surface. $\theta_{\mathrm{s}} = 140.7°$ is the azimuthal position of S, $\theta_{\mathrm{p}}$ is the azimuthal position of P and $\theta'$ is the azimuthal position of P′. $\varphi_{\mathrm{p}}$ and $\varphi'$ are the polar positions of P and P′, respectively.

In order to determine the coordinates of P, we define the location of the line connecting S and P′ as

$$\boldsymbol{L}(\boldsymbol{s}) = \boldsymbol{x}_{\mathrm{s}} + s(\boldsymbol{x}' - \boldsymbol{x}_{\mathrm{s}}), \tag{A. 6}$$

where $\boldsymbol{L}$ denotes the position of points on the line and $s$ is a parameter indicating distance along the line. Combining equations A.4 and A.5 with equation A.6, we can show that the radial coordinate of each point on the line $r_{\mathrm{L}} = |\boldsymbol{L}|$ is given by

$$r_{\mathrm{L}} = \{s^2[R^2 + (R+A)^2 - 2R(R+A)\sin\varphi' \cos(\theta' - \theta_{\mathrm{s}})] \\ + s[2R(R+A)\sin\varphi' \cos(\theta' - \theta_{\mathrm{s}}) - 2R(R+A)^2] + (R+A)^2\}^{1/2}. \tag{A. 7}$$

Next, we know that at P, $r_{\mathrm{L}} = R + h$, where $h$ is the altitude of P above the Earth's surface. So, defining $s_{\mathrm{p}}$ as the value of $s$ corresponding to the location of P, we can use equation A.7 to derive a quadratic equation for $s_{\mathrm{p}}$

$$s_{\mathrm{p}}^2[R^2 + (R+A)^2 - 2R(R+A)\sin\varphi' \cos(\theta' - \theta_{\mathrm{s}})] \\ + 2R(R+A)s_{\mathrm{p}}[\sin\varphi' \cos(\theta' - \theta_{\mathrm{s}}) - (R+A)] + (R+A)^2 - (R+H)^2 = 0. \tag{A. 8}$$

Solving equation A.8 produces two roots, the smallest of which corresponds to the position of P (the larger is a location on the opposite side of the Earth). Once the equation is solved, the position of P in Cartesian coordinates is given by

$$\boldsymbol{x}_{\mathrm{p}} = (x_{\mathrm{p}}, y_{\mathrm{p}}, z_{\mathrm{p}}) = \boldsymbol{L}(s = s_{\mathrm{p}}). \tag{A. 9}$$

These Cartesian coordinates are then converted back to spherical polar equivalents using

$$\varphi_{\mathrm{p}} = 90° + \sin^{-1}\left(\frac{z_{\mathrm{p}}}{R+h}\right), \tag{A. 10}$$

and

$$\theta_{\mathrm{p}} = \begin{cases} \tan^{-1}(y_{\mathrm{p}}/x_{\mathrm{p}}) & \text{if } x_{\mathrm{p}}, y_{\mathrm{p}} > 0 \\ 180° - \tan^{-1}(-y_{\mathrm{p}}/x_{\mathrm{p}}) & \text{if } x_{\mathrm{p}} < 0, y_{\mathrm{p}} > 0 \\ 180° + \tan^{-1}(y_{\mathrm{p}}/x_{\mathrm{p}}) & \text{if } x_{\mathrm{p}}, y_{\mathrm{p}} < 0 \\ 360° - \tan^{-1}(-y_{\mathrm{p}}/x_{\mathrm{p}}) & \text{if } x_{\mathrm{p}} > 0, y_{\mathrm{p}} < 0 \\ 90° & \text{if } x_{\mathrm{p}} = 0, y_{\mathrm{p}} > 0 \\ 270° & \text{if } x_{\mathrm{p}} = 0, y_{\mathrm{p}} < 0 \\ 0 & \text{if } x_{\mathrm{p}} > 0, y_{\mathrm{p}} = 0 \\ 180° & \text{if } x_{\mathrm{p}} < 0, y_{\mathrm{p}} = 0 \end{cases}, \tag{A. 11}$$

where $\varphi_{\mathrm{p}}$ and $\theta_{\mathrm{p}}$ are the polar and azimuthal coordinates of P. Additionally, in equation A.10, we have used the fact that, at all times, the umbrella cloud is in the southern hemisphere.

Finally, we convert these spherical polar coordinates back to latitude $\lambda_{\mathrm{lat}}$ and longitude $\lambda_{\mathrm{long}}$ using

$$\lambda_{\mathrm{lat}} = \varphi_{\mathrm{p}} - 90°, \tag{A. 12}$$

and

$$\lambda_{\mathrm{long}} = \begin{cases} 360° - \theta_{\mathrm{p}} & \text{if } \theta_{\mathrm{p}} > 180° \\ -\theta_{\mathrm{p}} & \text{if } \theta_{\mathrm{p}} < 180° \end{cases}. \tag{A. 13}$$

## References


Aizawa, K., Yokoo, A., Kanda, W., Ogawa, Y. & Iguchi, M., 2010. Magnetotelluric pulses generated by volcanic lightning at Sakurajima volcano, Japan. *Geophys. Res. Lett.*, 37(17), L17301. https://doi.org/10.1029/2010GL044208.

Aizawa, K., Cimarelli, C., Alatorre–Ilbarguengoitia, M. A., Yokoo, A., Dingwell, D. B. & Iguchi, M., 2016. Physical properties of volcanic lightning: Constraints from magnetotelluric and video observations at Sakurajima volcano, Japan. *Earth Planet. Sci. Lett.*, 444, 45-55. https://doi.org/10.1016/j.epsl.2016.03.024.

Amores, A., Monserrat, S., Marcos, M., Argueso, D., Villalonga, J., Jordà, G. & Gomis, D., 2022. Numerical simulation of atmospheric Lamb waves generated by the 2022 Hunga-Tonga volcanic eruption. *Geophys. Res. Lett.*, 49(6), e2022GL098240. https://doi.org/10.1029/2022GL098240.

Behnke, S. A., Thomas, R. J., McNutt, S. R., Schneider, D. J., Krehbiel, P. R., Rison, W. & Edens, H. E., 2013. Observations of volcanic lightning during the 2009 eruption of Redoubt Volcano. *J. Volcanol. Geotherm. Res.*, 259, 214-234. https://doi.org/10.1016/j.jvolgeores.2011.12.010.

Behnke, S. A., Edens, H. E., Thomas, R. J., Smith. C. M., McNutt, S. R., Van Eaton, A. R., Cimarelli, C. & Cigala, V., 2018. Investigating the Origin of Continual Radio Frequency Impulses During Explosive Volcanic Eruptions. *J. Geophys. Res. Atmos.*, 123(8), 4157-4174. https://doi.org/10.1002/2017JD027990.

Bielinski, T., 2020. A Parallax Shift Effect Correction Based on Cloud Height for Geostationary Satellites and Radar Observations. *Rem. Sens.*, 12, 365. https://doi.org/10.3390/rs12030365.

Bombrun, M., Jessop, D., Harris, A. & Barra, V., 2018. An algorithm for the detection and characterisation of volcanic plumes using thermal camera imagery. *J. Volcanol. Geotherm. Res.*, 352, 26-37. https://doi.org/10.1016/j.jvolgeores.2018.01.006.

Bonadonna, C., Genco, R., Gouhier, M., Pistolesi, M., Cioni, R., Alfano, F., Hoskuldsson, A. & Ripepe, M., 2011. Tephra sedimentation during the 2010 Eyjafjallajokull eruption (Iceland) from deposit, radar, and satellite observations. *J. Geophys. Res. Solid Earth*, 116(B12), B12202. https://doi.org/10.1029/2011JB008462.

Brenna, M., Cronin, S. J., Smith, I. E. M., Pontesilli, A., Tost, M., Barker, S., Tonga'onevai, S., Kula, T. & Vaiomounga, R., 2022. Post-caldera volcanism reveals shallow priming of an intraocean arc andesitic caldera: Hunga volcano, Tonga, SW Pacific. *Lithos*, 412-413. 106614. https://doi.org/10.1016/j.lithos.2022.106614.

Bryan, W. B., Strice, G. D. & Ewart, A., 1972. Geology, petrography and geochemistry of the volcanic islands of Tonga. *J. Geophys. Res.*, 77(8), 1566-1585. https://doi.org/10.1029/JB077i008p01566.

Carn, S. A., Krotkov, N. A., Fisher, B. L. & Li, C., 2022. Out of the blue: Volcanic SO2 emissions during the 2021-2022 eruptions of Hunga Tonga - Hunga Ha'apai (Tonga). *Front. Earth Sci.*, 10. https://doi.org/10.3389/feart.2022.976962.

Carr, J. L., Horvath, A., Wu, D. L. & Friberg, M. D., 2022. Stereo Plume Height and Motion Retrievals for the Record-Setting Hunga Tonga-Hunga Ha'apai Eruption of 15 January 2022. *Geophys. Res. Lett.*, 49(9), e2022GL098131. https://doi.org/10.1029/2022GL098131.

Carvajal, M., Sepulveda, I., Gubler, A. & Garreaud, R., 2022. Worldwide Signature of the 2022 Tonga Volcanic Tsunami. *Geophys. Res. Lett.*, 49(6), e2022GL098153. https://doi.org/10.1029/2022GL098153.

Cimarelli, C., Alatorre-Ibarguengoitia, M. A., Kueppers, U., Scheu, B. & Dingwell, D. B., 2014. Experimental generation of volcanic lightning. *Geology*, 42(1), 79-82. https://doi.org/10.1130/G34802.1.

Cimarelli, C., Alatorre-Ibarguengoitia, M. A., Aizawa, K., Yokoo, A., Díaz-Marina, A., Iguchi, M. & D. B. Dingwell, 2016. Multiparametric study of volcanic lightning: Sakurajima volcano, Japan. *Geophys. Res. Lett.*, 43(9), 4221-4228. https://doi.org/10.1002/2015GL067445.

Cimarelli, C. & Genareau, K., 2022. A review of volcanic electrification of the atmosphere and volcanic lightning. *J. Volcanol. Geotherm. Res.*, 422, 107449. https://doi.org/j.jvolgeores.2021.107449.

Colombier, M., Scheu, B., Wadsworth, F., Cronin, S., Vasseur, J., Dobson, K. J., Hess, K.-U., Tost, M., Yilmaz, T. I., Cimarelli, c., Brenna, M., Ruthensteiner, B. & D. B. Dingwell, 2018. Vesiculation and Quenching during Surtseyan Eruptions at Hunga Tonga-Hunga Ha'apai Volcano, Tonga. *J. Geophys. Res. Solid Earth*, 123, 3762-3779. https://doi.org/10.1029/2017JB015357.

Corradini, S., Guerrieri, L., Stelitano, D., Salerno, G., Scollo, S., Merucci, L., Prestifilippo, M., Musacchio, M., Silvestri, M., Lombardo, V. & Caltabiano, T., 2020. Near Real-Time Monitoring of the Christma 2018 Etna Eruption Using SEVIRI and Products Validation. *Rem. Sens.*, 12(8), 1336. https://doi.org/10.3390/rs12081336.

Costa, A., Folch, A. & Macedonio, G., 2013. Density-driven transport in the umbrella region of volcanic clouds: Implications for tephra dispersion models. *Geophys. Res. Lett.*, 40, 4823-4827. https://doi.org/10.1002/grl.50942.

Cronin, S. J., Brenna, M., Smith, I. E. M., Barker, S. J., Tost, M., Ford, M., Tonga'onevai, S., Kula, T. & Vaiomounga R., 2017. New volcanic island unveils explosive past. *EOS*, 98. https://doi.org/10.1029/2017EO076589.

Diaz Vecino, M. C., Rossi, E., Freret-Lorgeril, V., Fries, A., Gabellini, P., Lemus, J., Pollastri, S., Poulidis, A. P., Iguchi, M. & Bonadonna, C., 2022. Aerodynamic characteristics and genesis of aggregates at Sakurajima Volcano, Japan. *Sci. Rep.*, 12, 2044. https://doi.org/10.1038/s41598-022-05854z.

Fee, D., Steffke, A. & Garces, M., 2010. Characterization of the 2008 Kasatochi and Okmok eruptions using remote infrasound arrays. *J. Geophys. Res. Atmos.*, 115(D2), D00L10. https://doi.org/10.1029/2009JD013621.

Freret-Lorgeril, V., Donnadieu, F., Scollo, S., Provost, A., Fréville, P., Guehenneux Y., Hervier, C., Prestifilippo, M. & Coltelli, M., 2018. Mass Eruption Rates of Tephra Plumes During the 2011-2015 Lava Fountain Paroxysms at Mt. Etna From Doppler Radar Retrievals. *Front. Earth Sci.*, 6, 73. https://doi.org/10.3389/feart.2018.00073.

Freret-Lorgeril, V., Bonadonna, C., Rossi, E., Poulidis, A. P. & Iguchi, M., 2022. New insights into real-time detection of tephra grainsize, settling velocity and sedimentation rate. *Sci. Rep.*, 12, 4650. https://doi.org/10.1038/s41598-022-08711-1.

Garvin, J. B., Slayback, D. A., Ferrini, V., Frawley, J., Giguere, C., Asrar, G. R. & Andersen, K., 2018. Monitoring and Modeling the Rapid Evolution of Earth's Newest Volcanic Island: Hunga Tonga Hunga Ha'apai (Tonga) Using High Spatial Resolution Satellite Observations. *Geophys. Res. Lett.*, 45, 3445-3452. https://doi.org/0.1002/2017GL076621.

Gilbert, J. S., Lane, S. J., Sparks, R. S. J. & Koyaguchi, T., 1991. Charge measurements on particle fallout from a volcanic plume. *Nature*, 349, 598-600. https://doi.org/10.1038/349598a0.

Global Volcanism Program, 2022. Report on Hunga Tonga-Hunga Ha'apai (Tonga). In: Sennert, S. K. (ed.), Weekly Volcanic Activity Report, 12 January - 18 January 2022. Smithsonian Institute and US Geological Survey. https://volcano.si.edu/showreport.cfm?wvar=GVP. WVAR20220112-243040.

Gupta, A. K., Bennartz, R., Fauria, K. E. & Mittal, T., 2022. Eruption chronology of the December 2021 to January 2022 Hunga Tonga-Hunga Ha'apai eruption sequence. *Nat. Comms. Earth Environ.*, 3, 314. https://doi.org/10.1038/s43247-022-00606-3.

Gusman, A. R., Roger, J., Noble, C., Wang, X., Power, W. & Burbidge, D., 2022. The 2022 Hunga Tonga - Hunga Ha'apai volcano air-wave generated tsunami. *Pure Appl. Geophys*. https://doi.org/10.1007/s00024-022-03154-1.

Haney, M. M., Matoza, R. S., Fee, D. & Aldridge, D. F., 2017. Seismic equivalents of volcanic jet scaling laws and multipoles in acoustics. *Geophys. J. Int.*, 213(1), 623-636. https://doi.org/10.1093/gji/ggx554.

Inman, J. W., 1835. Navigation and Nautical Astronomy for the Use of British Seaman. C. and J. Rivington.

James, M. R., Lane, S. J. & Gilbert, J. S., 2000. Volcanic plume electrification: Experimental investigation of a fracture-charging mechanism. *J. Geophys. Res. Solid Earth*, 105(B7), 1664116649. https://doi.org/10.1029/2000JB900068.

James, M. R., Lane, S. J. & Gilbert, J. S., 2003. Density, construction, and drag coefficient of electrostatic volcanic ash aggregates *J. Geophys. Res. Solid Earth*, 108(B9), 2435. https://doi.org/10.1029/2002JB002011.

Johnson, C. G., Hogg, A. J., Huppert, H. E., Sparks, R. S. J., Phillips, J. C., Slim, A. C. & Woodhouse, M. J., 2015. Modelling intrusions through quiescent and moving ambients. *J. Fluid Mech.*, 771, 370-406. https://doi.org/10.1017/jfm.2015.180.

Jolly, A. D., Matoza, R. S., Fee, D., Kennedy, B. M., Iezzi, A. M., Fitzgerald, R. H., Austin, A. C. & Johnson, R., 2017. Capturing the Acoustic Radiation Pattern of Strombolian Eruptions using Infrasound Sensors Aboard a Tethered Aerostat, Yasur Volcano, Vanuatu. *Geophys. Res. Lett.*, 44, 9672-9680. https://doi.org/10.1002/2017GL074971.

Koyaguchi, T. & Woods, A. W. (1996). On the formation of eruption columns following explosive mixing of magma and surface-water. *J. Geophys. Res.*, 101(B3), 5561-5574. https://doi.org/10.1029/95JB01687.

Liu, X., Xu, J., Yue, J. & Kogure, M., 2022. Strong Gravity Waves associated with Tonga Volcano Eruption Revealed by SABER Observations. *Geophys. Res. Lett.*, 49(10), e2022GL098339. https://doi.org/10.1029/2022GL098339.

Mather, T. A. & Harrison, R. G., 2006. Electrification of volcanic plumes. *Surv. Geophys.*, 27, 387-432. https://doi.org/10.1007/s10712-006-9007-2.

Mastin, L. G. & Van Eaton, A. R., 2020. Comparing Simulations of Umbrella-Cloud Growth and Ash Transport with Observations from Pinatubo, Kelud, and Calbuco Volcanoes. *Atmosphere*, 11, 1038. https://doi.org/10.3390/atmos11101038.

Matoza, R. S., Le Pichon, A., Vergoz, J., Herry, P., Lalande, J.-M., Lee, H.-I., Che, I.-Y. & Rybin, A., 2011. Infrasonic observations of the June 2009 Sarychev Peak eruption, Kuril Islands: Implications for infrasonic monitoring of remote explosive volcanism. *J. Volcanol. Geotherm. Res.*, 200(1-2), 35-48. https://doi.org/10.1016/j.jvolgeores.2010.11.022.

Matoza, R. S., Fee, D., Assink, J. D., Iezzi, A. M., Green, D. N., Kim, K. et al., 2022. Atmospheric waves and global sesimoacoustic observations of the January 2022 Hunga eruption, Tonga. *Science*. https://doi.org/10.1126/science.abo7063.

McKee, K., Smith, C. M., Reath, K., Snee, E., Maher, S., Matoza, R. S., Carn, S., Mastin, L., Anderson, K., Damby, D., Roman, D. C., Degterev, A., Rybin, A., Chibisova, M., Assink, J. D., de Negri Levia, R. & Perttu, A., 2021. Evaluation the state of the art in remote volcanic eruption characterization Part I: Raikoke volcano, Kuril Islands. *J. Volcanol. Geotherm. Res.*, 419, 107354. https://doi.org/10.1016/j.jvolgeores.2021.107354.

McKee, K., Smith, C. M., Reath, K., Snee, E., Maher, S., Matoza, R. S., Carn, S., Roman, D. C., Mastin, L., Anderson, K., Damby, D., Itikarai, I., Mulina, K., Saunders, S., Assink, J. D., de Negri Levia, R. & Perttu, A., 2021. Evaluation the state of the art in remote volcanic eruption characterization Part II: Ulawun volcano, Papua New Guinea. *J. Volcanol. Geotherm. Res.*, 420, 107381. https://doi.org/10.1016/j.jvolgeores.2021.107381.

McNutt, S. R. & Thomas, R. J., 2015. Volcanic Lightning. In The Encyclopedia of Volcanoes 2nd Edition, 1059-1067. https://doi.org/10.1016/B978-0-12-385938-9.00062-6.

Omira, R., Ramalho, R. S., Kim, J., Gonzalez, P. J., Kadri, U., Miranda, J. M., Carrilho, F. & Baptista, M. A., 2022. Global Tonga tsunami explained by a fast-moving atmospheric source. *Nature*. https://doi.org/10.1038/s41586-022-04926-4.

Otsuka, S., 2022. Visualizing Lamb Waves From a Volcanic Eruption Using Meteorological Satellite Himawari-8. *Geophys. Res. Lett.*, 49, e2022GL098324. https://doi.org/10.1029/2022GL098324.

Pankhurst, M. J., Scarrow, J. H., Barbee, O. A., Hickey, J., Coldwell, B. C., Rollinson, G. K., Rodríguez-Losada, J. A., Martín Lorenzo, A., Rodríguez, F., Hernandez, W., Calvo Fernandez, D., Hernandez, P. A. and Pérez, N. M. (2022) Rapid response petrology for the opening eruptive phase of the 2021 Cumbre Vieja eruption, La Palma, Canary Islands. *Volcanica*, 5(1), 1–10. https://doi.org/10.30909/vol.05.01.0110.

Patrick, M. R., 2007. Dynamics of Strombolian ash plumes from thermal video: Motion, morphology, and air entrainment. *J. Geophys. Res.*, 112, B06202. https://doi.org/10.1029/2006JB004387.

Patterson, M. D., Simpson, J. E., Dalziel, S. B. & van Heijst, G. J. F., 2006. Vortical motion in the head of an axisymmetric gravity current. *Phys. Fluids*, 18, 046601. https://doi.org/10.1063/1.2174717.

Poli, P. & Shapiro, N., 2022. Rapid characterization of large volcanic eruptions: measuring the impulse of the Hunga Tonga explosion from teleseismic waves. *Geophys. Res. Lett.*, 49(8), e2022GL098123. https://doi.org/10.1029/2022GL098123.

Pollastri, S., Rossi, E., Bonadonna, C. & Merrison, J. P., 2021. Modelling the Effect of Electrification on Volcanic Ash Aggregation. *Front. Earth Sci.*, 8, 57. https://doi.org/10.3389/feart.2020.574106.

Pouget, S., Bursik, M., Johnson, C. G., Hogg, A. J., Phillips, J. C. & Sparks, R. S. J., 2016. Interpretation of umbrella cloud growth and morphology: implications for flow regimes of shortlived and long-lived eruptions. *Bull. Volc.*, 78, 1. https://doi.org/10.1007/s00445-015-0993-0.

Prata, A. T., Folch, A., Prata, A. J., Biondi, R., Brenot, H., Cimarelli, C., Corradini, S., Lapierre, J. & Costa, A., 2020. Anak Krakatau triggers volcanic freezer in the upper troposhere. *Sci. Rep.*, 10, 3584. https://doi.org/10.1038/s41598-020-60465-w.

Proud, S. R., Prata, A. & Schmauss, S., 2022. The January 2022 eruption of Hunga Tonga-Hunga Ha'apai volcano reached the mesosphere. Science, 378, 554-557. https://doi.org/10.1126/science.abo4076.

Schnepf, N. R., Minami, T., Toh, H. & Nair, M. C., 2022. Magnetic Signatures of the January 15 2022 Hunga Tonga-Hunga Ha'apai Volcanic Eruption. *Geophys. Res. Lett.*, 49(10), e2022GL098454. https://doi.org/10.1029/2022GL098454.

Schumacher, R., 1994. A reappraisal of Mount St. Helens' ash clusters - depositional model from experimental observations. *J. Volcanol. Geotherm. Res.*, 59(3), 253-260. https://doi.org/10.1016/03770273(94)90099-X.

Scollo, S., Boselli, A., Coltelli, M., Leto, G., Pisani, G., Spinelli, N. & Wang, X., 2012. Monitoring Etna volcanic plumes using a scanning LiDAR. *Bull. Volcanol.*, 74, 2383 - 2395. https://doi.org/10.1007/s00445-012-0669-y.

Self, S., Wilson, L. & Nairn, I. A., 1979. Vulcanian eruption mechanisms. *Nature*, 277, 440-443. https://doi.org/10.1038/277440a0.

Sellitto, P., Podglajen, A., R. Belhadji, Boichu, M., Carboni, E., Cuesta, J. et al., 2022. The unexpected radiative impact of the Hunga Tonga eruption of January 15th, 2022. *Nat. Comms. Earth Environ.*, 3, 288. https://doi.org/10.1038/s43247-022-00618-z.

Smith, C. M., Gaudin, D., Van Eaton A. R., Behnke, S. A., Reader, S., Thomas, R. J., McNutt, S. R. & Cimarelli, C., 2021. Impulsive Volcanic Plumes Generate Volcanic Lightning and Vent Discharges: A Statistical Analysis of Sakurajima Volcano in 2015. *Geophys. Res. Lett.*, 48(11), e2020GL09232. https://doi.org/10.1029/2020GL092323.

Tournigand, P.-Y., Taddeucci, J., Gaudin, D., Fernandez, J. J. P., Del Bello, E., Scarlato, P., Kueppers, U., Sesterhenn, J. Yokoo, A. (2017). The Initial Development of Transient Volcanic Plumes as a Function of Source Conditions. *J. Geophys. Res. Solid Earth*, 122, 9784-9803. https://doi.org/10.1002/2017JB014907.

Ungarish, M. & Zemach, T., 2007. On axisymmetric intrusive gravity currents in a stratified ambient - shallow-water theory and numerical results. *Eur. J. Mech. B*, 26, 220-235. https://doi.org/10.1016/j.euromechflu.2006.06.003.

Ungarish, M., Johnson, C. G. & Hogg, A. J., 2016. Sustained axisymmetric intrusions in a rotating system. *Eur. J. Mech. B*, 56, 110-119. https://doi.org/10.1016/j.euromechflu.2015.10.008.

UNOSAT, 2022. 15 January 2022 Volcanic Eruption and Tsunami. Preliminary Satellite-Based Comprehensive Damage Assessment Report. Tongatapu, Eua, and Ha'apai divisions of the Kingdom of Tonga. https://unosat-maps.web.cern.ch/TO/VO20220115TON/UNOSAT_ComprehensiveDamageAssessment_Tonga_20220204.pdf.

Van Eaton, A. R., Amigo, A., Bertin, D., Mastin, L. G., Giacosa, R. E., Gonzàlez, J., Valderrama, O., Fontijn, K. & Behnke, S. A., 2016. Volcanic lightning and plume behaviour reveal evolving hazards during the April 2015 eruption of Calbuco volcano, Chile. *Geophys. Res. Lett.*, 43(7), 3563-3571. https://doi.org/10.1002/2016GL068076.

Van Eaton, A. R., Schneider, D. J., Smith, C. M., Haney, M. M., Lyons, J. L., Said, R., Holzworth, R. H. & Mastin, L. G., 2020. Did ice-charging generate volcanic lightning during the 2016-2016 eruption of Bogoslof volcano, Alaska? *Bull. Volcanol.*, 82, 24. https://doi.org/10.1007/s00445-019-13505.

Van Eaton, A. R., Smith, C. M., Pavolonis, M. & Said, R., 2022. Eruption dynamics leading to a volcanic thunderstorm - The January 2020 eruption of Taal volcano, Philippines. *Geology*, 50(4), 491-495. https://doi.org/10.1130/G49490.1.

Vergoz, J., Hupe, P., Listowski, C., Le Pichon, A., Garces, M. A., Marchetti, E. et al., 2022. IMS observations of infrasound and acoustic-gravity waves produced by the January 2022 volcanic eruption of Hunga, Tonga: A global analysis. *Earth Planet. Sci. Lett.*, 591, 117639. https://doi.org/10.1016/j.epsl.2022.117639.

Woods, A. W. & Kienle, J., 1994. The dynamics and thermodynamics of volcanic clouds: Theory and observations from the April 15 and April 21, 1990 eruptions of Redoubt Volcano, Alaska. *J. Volcanol. Geotherm. Res.*, 62, 273-299. https://doi.org/10.1016/0377-0273(94)90037-X.

World Bank Group, 2022. The January 15, 2022 Hunga Tonga-Hunga Ha'apai eruption and tsunami, Tonga: Global Rapid Post Distaster Damage Estimation (GRADE) Report. https://thedocs.worldbank.org/en/doc/b69af83e486aa652d4232276ad698c7b-0070062022/original/GRADE-Report-Tonga-Volcanic-Eruption.pdf.

Wright, C. J., Hindley, N. P., Alexander, M. J., Barlow, M., Hoffmann, L., Mitchell, C. N., Prata, F., Bouillon, M., Carstens, J., Clerbaux, C., Osprey, S. M., Powell, N., Randall, C. E. & Yue, J., 2022. Surface-to-space atmospheric waves from Hunga Tonga-Hunga Ha'apai eruption. *Nature*, 609, 741-746. https://doi.org/10.1038/s41586-022-05012-5.

Yuan, Y. & Horner-Devine, A. R., 2013. Laboratory Investigation of the Impact of Lateral Spreading on Buoyancy Flux in a River Plume. *J. Phys. Oceanog.*, 43, 2588-2610. https://doi.org/10.1175/JPO-D-12-0117.1.

Yuen, D. A., Scruggs, M. A., Spera, F. J., Zheng, Y., Hu, H., McNutt, S. R., Thompson, G., Mandli, K., Keller, B. R., Wei, S. S., Peng, Z., Zhou, Z., Mulargia, F. & Tanioka, Y., 2022. Under the Surface: Pressure-Induced Planetary Scale Waves, Volcanic Lightning, and Gaseous Clouds Caused by the Submarine Eruption of Hunga Tonga-Hunga Ha'apai Volcano Provide and Excellent Research Opportunity. *Earthquake Research Advances*, 2(3), 100134. https://doi.org/10.1016/j.eqrea.2022.100134.